Simple convergent-nozzle aerosol injector for single-particle diffractive imaging with X-ray free-electron lasers

R. A. Kirian,[1,2,a)] S. Awel,[1,3,a)] N. Eckerskorn,[4] H. Fleckenstein,[1] M. Wiedorn,[1,5] L. Adriano,[6] S. Bajt,[6] M. Barthelmess,[1] R. Bean,[7] K. R. Beyerlein,[1] L. M. G. Chavas,[1] M. Domaracky,[1,8] M. Heymann,[1] D. A. Horke,[1] J. Knoska,[1,5] M. Metz,[1,5] A. Morgan,[1] D. Oberthuer,[1] N. Roth,[1] T. Sato,[1] P. L. Xavier,[1,5,9] O. Yefanov,[1] A. V. Rode,[4] J. Küpper,[1,3,5] and H. N. Chapman[1,3,5]

[1]*Center for Free-Electron Laser Science, DESY, 22607 Hamburg, Germany*
[2]*Department of Physics, Arizona State University, Tempe, Arizona 85287, USA*
[3]*Center for Ultrafast Imaging, University of Hamburg, 22761 Hamburg, Germany*
[4]*Laser Physics Centre, Research School of Physics and Engineering, Australian National University, Canberra, Australia*
[5]*Department of Physics, University of Hamburg, 22761 Hamburg, Germany*
[6]*Deutsches Elektronen-Synchrotron DESY, 22607 Hamburg, Germany*
[7]*European XFEL GmbH, 22761 Hamburg, Germany*
[8]*Faculty of Science, Pavol Jozef Šafárik University in Košice, Slovakia*
[9]*IMPRS-UFAST, Max-Planck Institute for Structure and Dynamics of Matter, 22761 Hamburg, Germany*

(Received 31 March 2015; accepted 18 May 2015; published online 19 June 2015)

A major challenge in high-resolution x-ray free-electron laser-based coherent diffractive imaging is the development of aerosol injectors that can efficiently deliver particles to the peak intensity of the focused X-ray beam. Here, we consider the use of a simple convergent-orifice nozzle for producing tightly focused beams of particles. Through optical imaging we show that 0.5 μm particles can be focused to a full-width at half maximum diameter of 4.2 μm, and we demonstrate the use of such a nozzle for injecting viruses into a micro-focused soft-X-ray FEL beam.

[http://dx.doi.org/10.1063/1.4922648]

I. INTRODUCTION

X-ray free-electron lasers (XFELs) offer a compelling new approach to imaging a wide variety of aerosolized particles at high resolution and under conditions that are not accessible through cryogenic electron microscopy or synchrotron-based X-ray microscopy. XFELs produce intense X-ray pulses of only a few tens of femtoseconds in duration, which are sufficient to overcome the fundamental resolution-limiting effects of X-ray radiation damage (Howells *et al.*, 2009) by making the illumination duration shorter than the time scale for the onset of significant atomic motion (Neutze *et al.*, 2000; Chapman *et al.*, 2006; Barty *et al.*, 2012; and Suga *et al.*, 2014). Diffraction patterns can be used to form images of targets without the need for lenses, and at resolutions limited, in principle, only by the X-ray wavelength [Hawkes and Spence, 2005; Nugent, 2010). Two dimensional sub-nanometer-resolution images should be achievable from single-shot diffraction patterns of irreproducible targets such as living cells and aerosol particles, and three-dimensional atomic-resolution structure determination should be possible by assembling many patterns from reproducible targets such as proteins and viruses

[a)]R. A. Kirian and S. Awel contributed equally to this work.

(each of which is destroyed completely by an XFEL pulse) (Bergh *et al.*, 2008). Since femtosecond pulses outrun atomic motion with timescales on the order of 10 fs, in principle, practically any target can be studied without the need for cryogenic cooling, which is usually required in electron microscopy (Frank, 2006) and X-ray microscopy (McDermott *et al.*, 2012) of biological samples. Time-resolved studies are also enabled, for example, by inducing structural changes with an optical laser that precedes an X-ray pulse (Tenboer *et al.*, 2014).

Coherent diffractive imaging of aerosols was first demonstrated at the FLASH soft-X-ray FEL facility (Bogan *et al.*, 2008) and has recently been extended to the hard-X-ray regime at facilities such as LCLS and SACLA. A wide variety of results have emerged in recent years, including images of RNA microsponges (Gallagher-Jones *et al.*, 2014), viruses (Seibert, 2011), cell organelles (Hantke *et al.*, 2014), and whole cells (van der Schot *et al.*, 2015). Three-dimensional structures have been determined from inorganic particles (Xu *et al.*, 2014) and viruses (Ekeberg, 2015). Aerosol particulates have been studied (Bogan *et al.*, 2010; Loh *et al.*, 2012), as have superfluid helium droplets (Gomez *et al.*, 2014), atomic clusters (Rupp *et al.*, 2014), small gas-phase molecules (Küpper, 2014), and metallic nanoparticles (Barke *et al.*, 2015).

XFEL-based imaging is best performed on isolated, substrate-free targets, in order to avoid scattered-photon noise and reduced contrast associated with surrounding materials such as liquid solvent or solid supports. XFEL pulse repetition rates are presently 100–120 Hz, and samples, therefore, must be replaced in rapid succession. X-ray focal spot diameters are typically in the range of 0.1–5 μm, and the rate at which X-rays intercept targets is of extreme importance since XFELs are costly large-scale facilities based on linear accelerators that are typically available to only one user group at a time. To this end, most femtosecond single-particle imaging experiments have utilized aerodynamic lens stacks (Murphy and Sears, 1964; Liu *et al.*, 1995; and Bogan *et al.*, 2008) in order to concentrate and inject particles into the vacuum environment of experimental end stations. These lens stacks consist of a series of concentric axis-symmetric apertures that cause particles to migrate toward the central streamline upon optimization of the relative magnitudes of particle inertial forces and gas-drag forces. As shown by Robinson (Robinson, 1956), particles in an incompressible and irrotational gas flow field generally tend to follow trajectories towards regions of higher density. Aerodynamic lens stacks are capable of producing collimated streams of protein-sized particles (of the order 5–30 nm in size) with particle beam diameters of a few hundred micrometers (Wang and McMurry, 2006b; Benner *et al.*, 2008). For particles such as large viruses (on the order of 30–500 nm), particle beams can be produced with diameters of just a few tens of micrometers (DiFonzo, 2000; Qi *et al.*, 2010). Formulae and software are available to assist in the design of aerodynamic lens stacks (Wang and McMurry, 2006a).

Experimental hit fractions (fraction of X-ray pulses that intercept a target) are proportional to the X-ray beam cross-section, and sub-micrometer dimensions are often required due to the need for very high intensity when imaging small, weakly scattering objects. Hit fractions are determined by the X-ray beam area and the projection of the particle-beam density along the X-ray beam. The projected particle beam density is inversely proportional to both the particle beam diameter and the speed of the particles, assuming a fixed rate at which particles exit the injector. One can improve the efficiency of XFEL experiments by reducing either of these parameters. As an example, hit fractions of about 80% have been achieved for a 5-μm-X-ray beam by Hantke *et al.* (2014), but this fraction would drop to 0.032% in the case of a 100-nm-X-ray beam and otherwise identical conditions, assuming that the hit fraction is proportional to the area of the X-ray beam. Notably, most of the hits reported by Hantke *et al.* were faint hits corresponding to particles located far from the center of the X-ray beam. If the particle beam was focused to dimensions smaller than the X-ray focus, even at the expense of higher particle speeds, the fraction of faint hits could be reduced significantly. Sample delivery efficiency (fraction of injected targets that are intercepted by an X-ray pulse) is another concern, since samples are often available only in small quantities and can be expensive to produce. Delivery efficiency is proportional to the hit fraction as well as the XFEL pulse repetition rate.

In this paper, we investigate the use of a compact single-orifice aerosol injector, operating with a 1 bar pressure difference between the injector and vacuum chamber, for XFEL

diffractive imaging experiments. Our design is motivated by extensive work spanning several decades (Israel and Friedlander, 1967; La Mora *et al.*, 1988; Fernandez de la Mora and Rosell-Llompart, 1989; and Mallina *et al.*, 1999) that show how sub- or super-sonic free-jet expansions into vacuum from a single capillary or convergent orifice can produce particle beams with either small angular divergence or tight focus. Slowly converging capillary injectors are also under investigation, mainly for the purpose of aerosol-based printing applications (Hoey *et al.*, 2012), and recent work has shown that nanoparticles can be focused to diameters of less than 2 μm (Akhatov *et al.*, 2008). As we show here, convergent nozzles are convenient due to their compact size (in our case, only about 1 mm in diameter and 20 mm long), are simple to fabricate and operate, and can maintain targets at atmospheric pressure until they rapidly exit into vacuum in less than 1 μs. Such injectors can produce tightly focused beams of sub-μm particles, with focal spots of about 5-μm diameter. Our experiments performed with a 1-μm diameter soft-X-ray FEL beam suggest the basic feasibility of utilizing such injectors for coherent diffractive imaging work.

II. INJECTOR DESIGN AND OPERATIONAL CONCEPT

The injector design considered here consists of a single converging nozzle orifice. Inside of the nozzle, where near-atmospheric pressure is maintained, particles closely follow the convergent gas streamlines. Outside of the nozzle, the gas freely expands into vacuum, and particles of sufficient momentum continue along their initial, radially inward trajectories. This focusing scheme is defined by the angle of the internal convergent nozzle walls, and results in particle trajectories that cross the nozzle's axis of symmetry at a nearly common point. We refer to this common crossover point as the "focal point" of the injector, but note that this point may vary slightly for particles that are initially located at different distances from the symmetry axis. Figure 1 shows the basic operational concept of the injector.

In our first experiments, described here, we used an injector with a convergence angle of 30 °, and an exit-orifice diameter of 100 μm. A central cross section through a 3D X-ray tomogram of the injector nozzle tip is shown in Figure 2(a). Ceramic nozzles were fabricated through an injection molding process (Small Precision Tools Inc.) using a mixture of corundum (Al_2O_3) and zirconia (ZrO_2). These nozzles had an overall length of 20 mm, an inner diameter of 0.5 mm, and an outer diameter of 1 mm. Aerosolized particles were produced with a gas-dynamic virtual nozzle (GDVN) (DePonte, 2008), which typically generated droplets of about

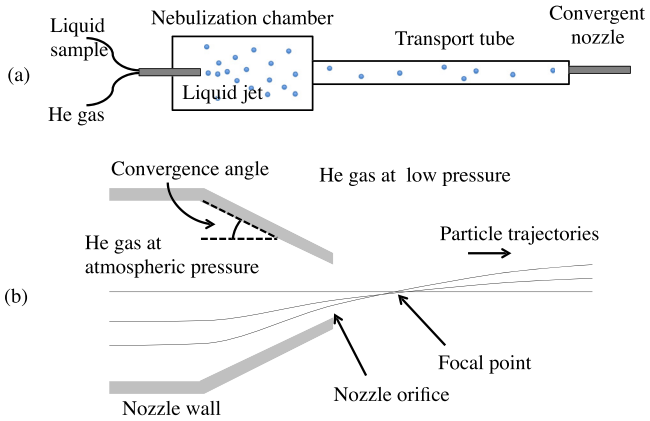

FIG. 1. (a) Schematic of the aerosol injector assembly and convergent nozzle. Liquid drops are formed in a nebulization chamber via a gas-dynamic virtual nozzle, which then pass through a transport tube before reaching the convergent nozzle depicted in (b). Particle trajectories closely follow the gas streamlines within the convergent nozzle, which is at near-atmospheric pressure. Upon exiting the nozzle, the pressure suddenly drops, and the ejected high-speed particles follow nearly straight-line trajectories, though they may accelerate slightly upon exiting. All particles cross over the nozzle's axis of symmetry at a common focal point that varies only slightly with the initial position of the particles at the exit orifice. The slightly curved trajectories of particles exiting the nozzle are exaggerated for illustrative purposes.

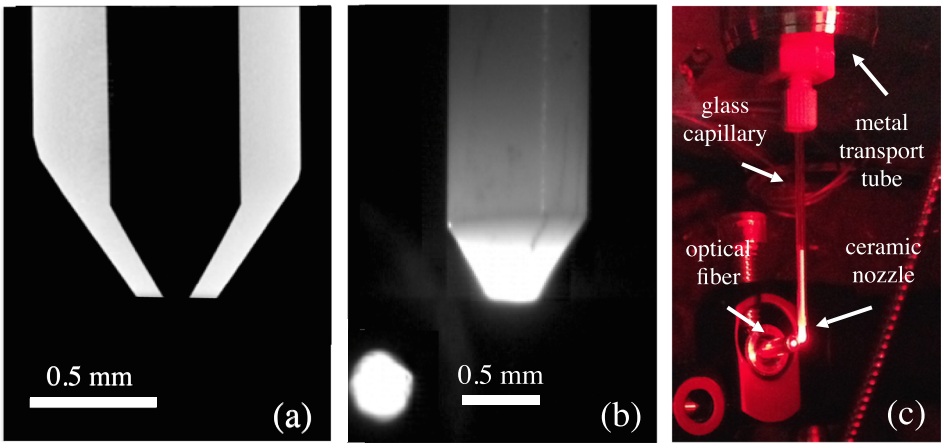

FIG. 2. (a) The cross section of a ceramic injector tip obtained through x-ray tomography, which shows the 30° convergent cone and exit orifice of 100-μm diameter. (b) Image of the ceramic injector tip. (c) Image showing the nozzle mounted to the transport tube in vacuum. The end of a 400-μm-diameter fiber optic used for illuminating particles is shown to the left of the injector tip.

1–1.5 μm diameter at a liquid flow rate of about 1–3 μl/min, and a gas mass-flow rate of about 20 mg/min (gas and liquid pressures of about 20–50 bars are typical). The GDVN was housed in a nebulization chamber with inner diameter of about 4 cm and length of about 12 cm. The aerosolized particles passed through a metal tube of 70 cm length and 2.8 cm inner diameter, onto which the nozzle was fixed. The small ceramic tip was epoxied to a glass capillary for ease of mounting. The pressure in the nebulization chamber was monitored with a dial gauge and was typically within about 20% of atmospheric pressure, depending on the flow rate of the liquid-focusing gas in the GDVN. The pressure did not rise far above atmosphere in general, since a one-way valve was used to avoid over pressurization and possible rupture of the nebulization chamber. We used helium as the carrier gas in order to minimize X-ray scattering, and because GDVNs tend to perform best with a lightweight monatomic gas. The use of helium as the carrier gas also increases the particle inertia (as compared to N_2, for example) and thereby facilitates focusing of smaller particles. Figures 2(b) and 2(c) show the injector mounted inside of the vacuum chamber, with a magnified view of the nozzle tip.

Our choice of nozzle geometry and orifice diameter was based on the components that were available to us for these first experiments. We chose an atmospheric pressure condition within the nozzle both for simplicity and to maintain samples in physiological conditions. Due to the large pressure difference between the aerosol delivery tube and the chamber, the flow through the nozzle is assumed to be choked. In this condition, the exit velocity of the helium gas is limited to the speed of sound, and further reductions in the chamber pressure below 0.4 bar will have no effect on this speed. For a 100-μm orifice, we estimate that the mass-flow rate for helium at atmospheric pressure upstream is 60 mg/min, which is similar to the typical 10–100 mg/min flow rates of our GDVN nozzles. Under this condition, the exiting gas velocity at the centerline of the nozzle reaches values near Mach 1 (Israel and Friedlander, 1967), approximately 1000 m/s for helium at standard temperature and pressure. Due to the abrupt convergence of the nozzle, particles of sufficiently large aerodynamic size may not have sufficient time to reach their terminal velocity, which is desirable since hit fractions are inversely proportional to the speed of the particle stream.

In nearly all aerodynamic focusing schemes, the parameter of greatest importance is the Stokes number, defined as $S = v_g\tau/D$, where τ is the particle relaxation time or the inverse of the proportionality constant between viscous acceleration of the particle and the difference between particle and gas velocities; $\tau\frac{\partial^2 \boldsymbol{v}_p}{\partial t^2} = \boldsymbol{v}_g - \boldsymbol{v}_p$, where $\boldsymbol{v}_p$ is the particle velocity

(Rao *et al.*, 1993). The relaxation time is equal to $\tau = \frac{\rho_p D_p^2 C}{18\mu_g f}$, where ρ_p is the particle density, D_p is the particle diameter, and the parameters C and f are correction factors that depend on particle Knudsen number (ratio of gas mean-free path to particle diameter) and Reynolds number (Liu *et al.*, 1995). The Stokes number for our nozzle, with 0.5-μm-diameter particles of density 1.05 g/cm^3, is approximately equal to 17. The critical Stokes number, at which particle beams are focused at infinity, is typically $S \approx 1$, although this depends on the exact nozzle geometry (Fuerstenau *et al.*, 1994; Liu *et al.*, 1995). The relaxation time for a 0.5-μm-diameter polystyrene particle (density $\rho_p \approx 1.05$ g/cm^3) in atmospheric helium is approximately equal to 3.5 μs, which, as we show below, is longer than the 750 ns that it takes for the particle to reach the focal point at a distance of 205 μm from the injector tip.

Similar flow fields can be achieved when scaling the present design in overall size while constraining the nozzle Reynolds number $Re = \rho_g v_g D/\mu_g \approx 940$, where $\rho_g \approx 0.18$ kg/m^3 is the helium gas density, $v_g \approx 1,000$ m/s is the assumed average gas velocity at the nozzle exit plane, $D \approx 1 \times 10^{-4}$ m is the nozzle orifice diameter, and $\mu_g \approx 1.9 \times 10^{-5}$ Pa s is the viscosity of helium at standard temperature and pressure. This Reynolds number is significantly larger than that of an aerodynamic lens stack consisting of several thin-plate orifices, which are typically limited to $Re < 100$ in order to avoid turbulent flow conditions (Vidal-de-Miguel and de la Mora, 2012). Indeed, the work of Rao *et al.* (1993) showed that for values of Re down to at least 15, the aerodynamic focusing effect for convergent nozzles is fairly insensitive to Re. An enlarged nozzle geometry would reduce the potential for nozzle clogging, increase the focal length of the converging aerosol beam, thus placing the X-ray beam further away from the nozzle end, and reduce the particle speeds. However, the particle-beam focus may increase with increasing nozzle size due to geometric aberrations, and the effects of diffusion may become significant.

III. OPTICAL IMAGING AND INJECTOR PERFORMANCE

Our injector was first tested through direct imaging-based measurements of particle velocities and projected particle beam density. A compact pulsed-laser illumination scheme was implemented using a red diode laser of 635-nm wavelength and 10-W average power (DILAS model M1F4S22) coupled to a multi-mode fiber of 400 μm core diameter. The diode laser was pulsed with a custom-built driver (Dr. Heller Elektronik) that generated 100 ns pulses with a top-hat temporal profile at repetition rates up to 100 kHz. The end of the fiber optic was situated near to the injector tip without focusing optics, and we imaged in a quasi-dark-field mode by setting the angle of the fiber optic such that the direct beam did not enter the imaging objective. We used a high-frame-rate CMOS camera (Photron SA4) and a 10× long-working-distance objective (Edmund Optic 46-144) to record images. The objective was mounted in the vacuum chamber at a working distance of about 33.5 mm, and the image projected through a window directly onto the camera sensor located outside of the chamber. This configuration proved to be sufficient for visualizing scattered light from fast-moving polystyrene particles of diameter down to about 200 nm. Smaller particles can be imaged provided an imaging chip with higher sensitivity or a laser of higher intensity, e.g., with ~10 W average power albeit at lower pulse repetition rate, as will be discussed in a subsequent report that details this, and other, optical imaging configurations (Awel *et al.*, unpublished). We note that in individual exposures we can remove background signal and determine the centroid of an isolated particle at a resolution better than the imaging resolution (Chang *et al.*, 1998). Since the single-snapshot images do indeed contain a sparse field of particles, the resolution to which we characterize the projected particle beam profile is likewise at high resolution, akin to the blink microscopy technique of photoactivated localization microscopy (Betzig *et al.*, 2006).

Figure 2 shows the fiber optic situated nearby the injector tip, and Figure 3 shows a sum of 100 images, each with exposures by 5 laser pulses. Particle streaks in this image correspond to a 100-ns-duration exposure. The velocity of the particles can be inferred from the streak length, which was typically 261±23 m/s for 500 nm particles and 280±11 m/s for 200-nm-diameter particles. Relative particle densities can be estimated by identifying particles as elongated

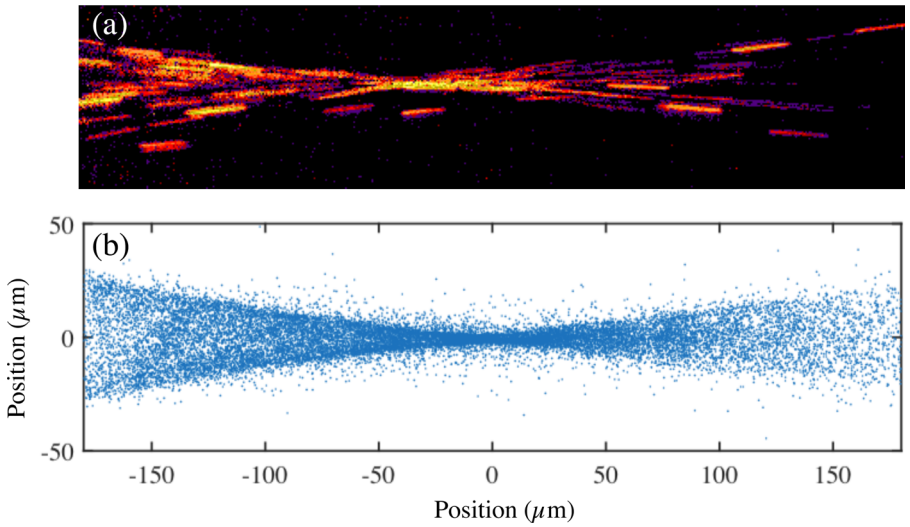

FIG. 3. (a) A sum of 500 exposures of 100-ns duration laser illumination, revealing streaks from 500-nm diameter particles. (b) Particle positions determined from streak intensity centroids from 43 000 images, each with 5 laser pulses.

groups of connected pixels that fall above a configurable threshold. The centroids of identified particle streaks shown in Figure 3 were assumed to be representative of particle positions, and we presume that this measure is reasonably accurate even for slightly out-of-focus particle images (the depth of focus for our objective is 3.5 μm). The particle density maps shown in Figure 4 were formed from particle positions obtained in about 43 000 exposures recorded at 1 kHz frame rate (processing on a desktop computer took about 5 min). The densities shown in these maps have been scaled to represent the condition in which particles enter the injector at a rate of 1 MHz, by using the known particle concentration and flow rates along with the number of laser pulses per camera exposure. Specifically, we multiplied the raw histogram counts by $1\text{MHz}/(cQN_f)$, where c is the volume concentration of the sample, Q is the volumetric flow rate of the liquid jet, and N_f is the total number of laser flashes that contributed to the histogram. While these density maps may not be true 2D projections throughout the imaging plane, the assumption of a projection is reasonable near the focus of the particle stream. Transmission efficiencies may be calculated using the expression $n = fl/v$, where n is the total number of

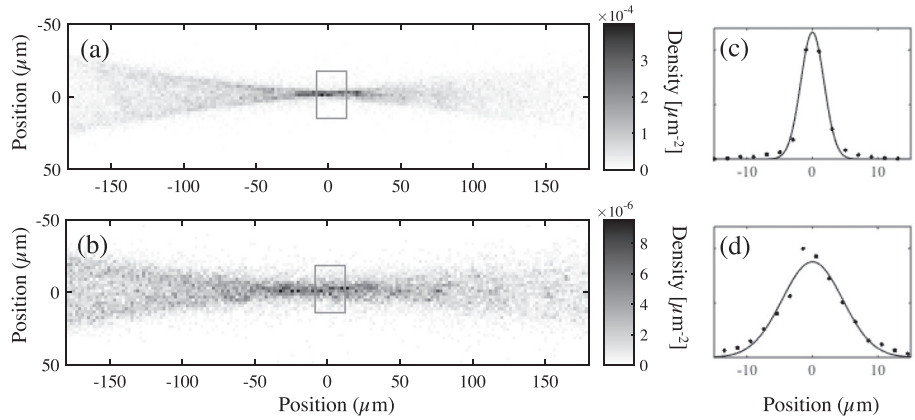

FIG. 4. (a) and (b) Histograms formed from particle positions for 500 and 200 nm latex sphere, respectively. As described in the main text, the units of μm^{-2} here correspond to conditions in which particles are introduced into the injector at a rate of 1 MHz. (c) and (d) Gaussian fits to the focal regions (gray boxes drawn in (a) and (b)) of the density histograms.

particles expected to lie within a slab of thickness l when particles are injected at a frequency f at a fixed velocity v in the direction normal to the slab. By comparing the calculated value of n for 100% transmission against the value of n measured by the histrograms, we estimate that the lower bounds on transmission efficiencies were $18 \pm 3\%$ and $0.12 \pm 0.02\%$ for the cases of 500 nm and 200 nm particles, respectively. We have no explanation for the large discrepancy in the transmission efficiency between the two particle sizes, but note that we have made no effort to optimize for transmission, and our particle-identification algorithm has not been optimized to identify every particle (it rejects particle images with low signal-to-noise ratio, and overlapping streaks that fail to meet the maximum length criterion, for example).

The focal point of the particle beam was approximately 205 μm from the nozzle orifice, which the particles reach within about 750 ns after exiting the nozzle. This focal length is rather close to the distance of 187 μm that one would expect from a purely geometric focusing based on the 30° convergence angle of the nozzle (we presume that the longer observed distance may be attributed to the acceleration of particles upon exiting, as drawn qualitatively in Fig. 1). The throat diameter of the particle beam, outside of which there are few observed particles, is nearly half the diameter of the orifice, similar to previous observations (Fuerstenau *et al.*, 1994). The FWHM diameter of the particle beams, determined by fitting a Gaussian profile to the focal region of the particle density maps, was 4.2 μm for 500 nm particles and 10.8 μm for 200 nm particles (see Figure 4). The pressure of the vacuum chamber was maintained at about 0.5 mbar. As predicted by our assumption of choked flow, we did not observe measureable differences in particle speed or density profile when this pressure was increased or decreased by a factor of 10.

Clogging is an important concern when using exit orifices of such small diameter. At the same time, it is likely that small focal spots will correspond to small orifices, so a practical compromise must be made. Cumulatively, the experiments that we have performed so far amount to about 20 h of operation, and over this time period we have encountered clogging issues twice. On the occasions that we observed these clogs, we noticed that the liquid jet was producing noticeably larger droplets than in ideal operation, suggesting that clogs may be averted by careful online observation of the aerosol droplets, perhaps through Mie scattering measurements, or by rejection of large droplets. The optical imaging results described above utilized solutions of polystyrene particles suspended in 2 mM sodium azide at a concentration of 0.04% solids by mass and flow rates of 2 μl/min, which for our nozzle pressure of 45 bars corresponds to droplet diameters of about 1.3 μm (Ganan-Calvo, 1998). Since these droplets are smaller than the 2-μm resolution of our optical microscope, we could not confirm the droplet size at their origin just downstream of the GDVN. For 200 nm particles, it is likely that many droplets contained more than one sphere since we estimate that there were 0.9 spheres per droplet on average. For 500-nm particles, we estimate that there were 0.06 spheres per droplet. We repeatedly observed that no particles were detected at the convergent nozzle exit when pure water or buffer was flown through the GDVN nozzle. Droplet evaporation is facilitated by the fact that the mass flow rate of helium exceeds the mass flow rate of liquid by about one order of magnitude, which helps avoid water vapor saturation.

IV. FEL DIFFRACTION EXPERIMENTS

We tested the feasibility of using our injector for diffractive imaging purposes at the FLASH soft-X-ray FEL facility in Hamburg, Germany. For these experiments, samples of Cydia pomonella granulovirus (CpGV) (Jehle *et al.*, 2006) suspended in water at a concentration of 10^{11} particles ml^{-1} were used for injection. CpGV is a baculovirus that infects invertebrates such as the Codling moth (*Cydia pomonella*). In these viruses, a single virion, containing the viral genome, is natively embedded in an occlusion body (OB), an *in vivo* grown polyhedrin protein crystal with a nominal size of $200 \times 200 \times 400\,\mathrm{nm}^3$. The virus crystals show a narrow size/shape distribution, as can be seen in Figure 5. The injector system described above was mounted to the diffractive imaging chamber, which was maintained at a pressure of about 5×10^{-5} mbar. The laser-imaging system described previously was not available during these

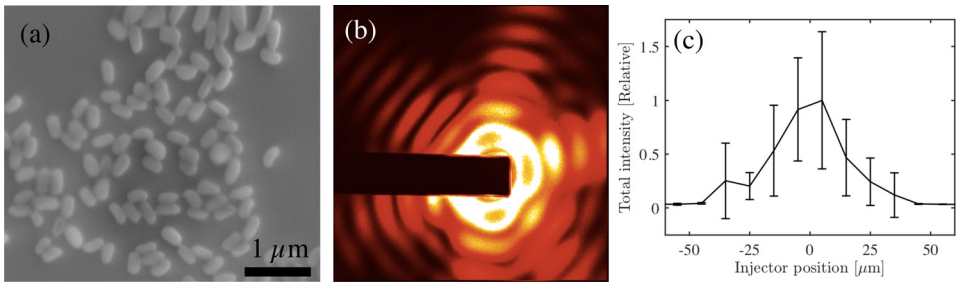

FIG. 5. (a) A scanning electron microscope image of granulovirus particles. (b) A single-shot diffraction pattern from an isolated granulovirus, isolated from the much greater number of aggregated particle clusters. (c) A plot of the average total diffracted x-ray photon counts as a function of injector position. Error bars indicate the standard deviation in each measurement.

measurements, which necessitated a time-consuming scanning approach in order to overlap the X-ray and particle beam.

The FLASH FEL is capable of producing pulse trains composed of an arbitrary number of pulses between 1 and 400, spaced with regular 1 μs intervals. These pulse trains repeat at 10 Hz frequency. The FEL beam was tuned to a wavelength of 13.45 nm, and produced pulses of 70 ± 20 μJ energy. X-rays were focused to a diameter of approximately 1 μm by a multi-layer-coated off-axis parabola with 27-cm focal length (Bajt *et al.*, 2009; Nelson *et al.*, 2009). Diffraction patterns were recorded on a Princeton Instrument MTE 2048B CCD (2048×2048 pixels, each 13.5 μm in size, 4-s full-frame readout) situated at a sample-to-detector distance of approximately 7 cm. The defocused direct X-ray beam was blocked by a 3-mm-thick Cu beam stop.

In order to overlap the X-ray focus with the particle beam, we collected data in a many-shot mode in which the X-ray CCD integrated the diffraction signal from many-shot pulse trains. Binned images were read out at a rate of 2 frames/s. We monitored hit rates on-line using a simple threshold criterion on the diffraction intensity while translating the injector via motorized translation stages. As hit rates approached 100%, we reduced the number of pulses in each train, eventually reaching the point of single-pulse operation. Approximately 2.5 h were spent on locating the particle beam. Figure 5 shows a single-pulse diffraction pattern from an isolated granulovirus near the focus of the X-ray beam. The two prominent fringe spacings in this diffraction pattern correspond to 400 nm and 313 nm lengths, which agrees well with images of individual granulovirus particles. Image reconstructions were not possible due to the loss of low-spatial-frequency information contained in the beamstop and in the saturated regions seen in the second diffraction peak.

The injector was operated continuously for a total of 4.5 h, and over the course of the final 1.9 h of our experiment we performed several one-dimensional scans of the injector position such that the particle beam crossed the X-ray beam. These scans were performed for two different distances between the X-ray beam and the nozzle tip, which we roughly estimated were at about 300 and 450 μm downstream from the nozzle tip. We estimate that the smallest particle-beam width across which we scanned the X-ray beam was 30 μm FWHM, as determined by plotting the average integrated intensity from 100-pulse exposures as a function of injector position (see Figure 5(c)). Near this location, an average hit fraction of 18% was estimated from a collection of single-pulse measurements by assuming that all patterns with an integrated intensity above 3σ intercepted a particle, where σ is the standard deviation of integrated intensities for blank frames. This measure utilized a total of 99 frames that fell within a 30-μm window centered at the nominal particle beam focus. By visual inspection, about 90% of diffraction patterns appeared to arise from virus particle clusters. This is likely caused by the droplet size from the liquid jet being too large for the sample concentration. During these measurements, it is estimated that droplets of a few micrometers in diameter were produced from a nozzle running at a liquid flow rate of 3.5 μl/min, which would indeed result in more than one virus in each drop on average. Nearly all diffraction patterns exhibited a high degree of contrast and

asymmetry, which suggests that most of the liquid from the initial droplets had evaporated prior to reaching the convergent nozzle exit (we would otherwise observe rather symmetric diffraction patterns consistent with nearly spherical objects).

Altogether, the data we collected during this experiment were very limited by the total available beamtime. While we observed a large fraction of aggregated particle clusters, we note that the mechanism for generating and conditioning the initial aerosol particle suspension is largely independent of the particle focusing mechanism that we describe here. An electrospray nebulization source, for example, can produce initial droplets that are about an order of magnitude smaller, and with number densities much higher, than the droplets produced by a typical GDVN.

V. DISCUSSION AND CONCLUSIONS

Our optical imaging experiments have shown that a simple convergent nozzle can focus low-density nanoparticle beams to FWHM diameters of 4.2 and 10.8 μm, for particle diameters of 500 and 200 nm, respectively. We also demonstrated that such nozzles can be used to inject $200 \times 200 \times 400\text{-nm}^3$ virus particles into the 1-μm focus of a soft-X-ray FEL. The question of how a convergent nozzle compares against an aerodynamic lens stack naturally arises, and we emphasize that these two injectors *differ* in many respects, and therefore can only be compared directly when a particular set of particle and pressure constraints are imposed. While the present work is by no means intended to conclude that convergent nozzles are better-suited to XFEL diffractive imaging in general, we wish to identify the many motivations for their continued development. The size and shape of the nozzle we tested here are practically identical to that of a liquid-jet nozzle, and therefore one can utilize the same basic hardware infrastructure for imaging experiments based on both liquid-jet and aerosol injection, with little time needed to switch between configurations. The use of a small nozzle also suggests the feasibility of mass fabrication through injection-molding techniques, as well as the consideration of acoustically pulsing the ejection of particles, which, when synchronized with the X-ray beam, could lead to significant improvements to sample delivery efficiency. Due to the small 100-μm apertures of the nozzles we tested, we were able to operate at atmospheric pressure within the nozzle, which may be advantageous for targets that must be maintained at nearly physiological temperatures and pressures.

We observed particle speeds in the range of about 230–300 m/s for particles in the range of 0.2–0.5 μm diameter, which is somewhat greater than the roughly 100-m/s speeds measured with aerodynamic lens stacks (Benner *et al.*, 2008). However, this speed increase is accompanied by a reduced particle beam diameter—if velocity increases in proportion to beam diameter, hit rates will be unaffected since this quantity scales inversely with both velocity and beam diameter. Our smallest observed beam diameter of 4.2 μm is considerably smaller than that achieved with aerodynamic lenses by more than the ratio of two of the particle velocity in the converging nozzle to that of the aerodynamic lens, suggesting that hit fractions should be higher than for aerodynamic lenses. Increased speeds may even be of advantage in some cases, for example, at high-repetition-rate XFELs where high-energy debris from intercepted particles must be rapidly cleared away before a subsequent X-ray pulse arrives, and pre-exposure of upstream particles by the extended profile of the intense X-ray beam may cause radiation damage. In the case of tightly focused particle beams that are comparable to the size of the X-ray beam, the fraction of diffraction patterns arising from faint regions of the X-ray beam could be reduced significantly.

The cost associated with the tight focus of a convergent aerosol beam is that maximizing the hit rate requires a three-dimensional scan of the injector position relative to the convergent X-ray focus, rather than a two-dimensional scan needed for a collimated particle beam (produced, for example, by an aerodynamic lens stack). We found this to be a significant challenge in our soft-X-ray FEL measurements. However, we have demonstrated a laser illumination system that can likely remedy this problem, with the added benefit of direct on-line imaging of the aerosol beam that would allow one to rapidly identify and diagnose injector problems, as well

as optimize the sample injector for highest projected particle density (Awel *et al.*, unpublished). It should be noted that the offline optimization of particle beam diameter alone does not necessarily optimize the hit fraction since factors such as particle velocity and transmission efficiency are also important. Direct imaging is a straightforward and non-invasive means of determining such parameters independently, although, ultimately, a projected particle density is the only measurement needed to estimate hit fractions.

The conditions that we investigated here, namely, atmospheric pressure and a small choked-flow orifice, worked particularly well for particles of 0.5–μm diameter over periods of several hours. We observed that smaller particles of 0.2-μm diameter did not focus as well, and we expect this trend to continue with decreasing diameter since the focusing mechanism is strongly dependent on the particle's momentum. In order to maintain atmospheric pressure upstream of the orifice, and simultaneously maintain the chamber pressure at sufficiently low pressure for nanoparticle imaging, it is likely that a smaller orifice is required to achieve adequate focusing. Clogging issues may arise for significantly smaller orifices, and therefore one might instead reduce the pressure in the nozzle in order to focus smaller particles.

Our present convergent nozzle injects gas into the experimental chamber at a higher mass flow rate than an aerodynamic lens stack, since lens stacks operate at lower pressures and necessitate pumping away part of the initial gas load. The increased gas density at the injector exit raises possible concerns regarding the background scatter from the evaporated buffer solution. We estimate that the total scattering from water vapor and helium is about two orders of magnitude lower than the total scattering from a 100-nm virus, assuming a 100-nm x-ray beam with 4 keV photon energy and the flow conditions presented above. Acceptable operational conditions will be strongly dependent on resolution, particle size, and x-ray beam diameter.

Our first proof-of-principle demonstration of a convergent nozzle for soft-X-ray FEL-based nanoparticle imaging was very encouraging. Despite the limited time available for this study, we observed a high hit rate from a beam of viruses with a minimum diameter of 30-μm-FWHM. Given this observation, combined with our optical measurements, we believe that convergent nozzles are a promising pathway toward increased high-intensity hit rates, from samples maintained at atmospheric conditions, with a relatively simple injector.

ACKNOWLEDGMENTS

We thank J. Bielecki, K. Mühlig, and J. Hajdu for help with the FLASH experiment. Tomographic measurements were carried out with the assistance of F. Wilde using an instrument of the P05 beamline in the Max von Laue Petra III experimental hall located at DESY. Granulovirus samples were provided by J. Jehles. In addition to DESY, this work has been supported by the excellence cluster "The Hamburg Center for Ultrafast Imaging—Structure, Dynamics and Control of Matter at the Atomic Scale" of the Deutsche Forschungsgemeinschaft (CUI, DFG-EXC1074). This research was partially supported under Australian Research Council's Discovery Projects funding scheme (Project No. DP110100975). J. Küpper acknowledges support by the European Research Council through the Consolidator Grant 614507-COMOTION. R.A.K. acknowledges support from the NSF STC Award 1231306.

Akhatov, I. S., Hoey, J. M., Swenson, O. F., and Schulz, D. L., "Aerosol flow through a long micro-capillary: Collimated aerosol beam," Microfluid. Nanofluid. **5**(2), 215–224 (2008).

Awel, S., Kirian, R. A., Eckerskorn, N., Wiedorn, M., Rode, A. V., Küpper, J., and Chapman, H., "Visualizing aerosol-particle injection for diffractive-imaging experiments" (unpublished).

Bajt, S., Chapman, H. N., Nelson, A. J., Lee, R. W., Toleikis, S., Mirkarimi, P., Alameda, J., Baker, S. L., Vollmer, H., Graff, R. T., Aquila, A., Gullikson, E. M., Meyer Ilse, J., Spiller, E., Krzywinski, J., Juha, L., Chalupský, J., Hájková, V., Hajdu, J., and Tschentscher, T., "Sub-micron focusing of soft x-ray free electron laser beam," Proc. SPIE **7361**, 73610J (2009).

Barke, I., Hartmann, H., Rupp, D., Flückiger, L., Sauppe, M., Adolph, M., Schorb, S., Bostedt, C., Treusch, R., Peltz, C., Bartling, S., Fennel, T., Meiwes-Broer, K.-H., and Möller, T., "The 3D-architecture of individual free silver nanoparticles captured by x-ray scattering," Nat. Commun. **6**, 6187 (2015).

Barty, A., Caleman, C., Aquila, A., Timneanu, N., Lomb, L., White, T. A., Andreasson, J., Arnlund, D., Bajt, S., Barends, T. R. M., Barthelmess, M., Bogan, M. J., Bostedt, C., Bozek, J. D., Coffee, R., Coppola, N., Davidsson, J., DePonte, D. P., Doak, R. B., Ekeberg, T., Elser, V., Epp, S. W., Erk, B., Fleckenstein, H., Foucar, L., Fromme, P., Graafsma, H., Gumprecht, L., Hajdu, J., Hampton, C. Y., Hartmann, R., Hartmann, A., Hauser, G., Hirsemann, H., Holl, P., Hunter, M.

S., Johansson, L., Kassemeyer, S., Kimmel, N., Kirian, R. A., Liang, M., Maia, F. R. N. C., Malmerberg, E., Marchesini, S., Martin, A. V., Nass, K., Neutze, R., Reich, C., Rolles, D., Rudek, B., Rudenko, A., Scott, H., Schlichting, I., Schulz, J., Seibert, M. M., Shoeman, R. L., Sierra, R. G., Soltau, H., Spence, J. C. H., Stellato, F., Stern, S., Strueder, L., Ullrich, J., Wang, X., Weidenspointner, G., Weierstall, U., Wunderer, C. B., and Chapman, H. N., "Self-terminating diffraction gates femtosecond x-ray nanocrystallography measurements," Nat. Photonics **6**(1), 35–40 (2012).

Benner, W. H., Bogan, M. J., Rohner, U., Boutet, S., Woods, B., and Frank, M., "Non-destructive characterization and alignment of aerodynamically focused particle beams using single particle charge detection," J. Aerosol Sci. **39**(11), 917–928 (2008).

Bergh, M., Huldt, G., Timneanu, N., Maia, F. R. N. C., and Hajdu, J., "Feasibility of imaging living cells at subnanometer resolutions by ultrafast x-ray diffraction," Q. Rev. Biophys. **41**(3–4), 181–204 (2008).

Betzig, E., Patterson, G. H., Sougrat, R., Lindwasser, O. W., Olenych, S., Bonifacino, J. S., Davidson, M. W., Lippincott-Schwartz, J., and Hess, H. F., "Imaging intracellular fluorescent proteins at nanometer resolution," Science **313**(5793), 1642–1645 (2006).

Bogan, M. J., Benner, W. H., Boutet, S., Rohner, U., Frank, M., Barty, A., Seibert, M. M., Maia, F., Marchesini, S., Bajt, S., Woods, B., Riot, V., Hau-Riege, S. P., Svenda, M., Marklund, E., Spiller, E., Hajdu, J., and Chapman, H. N., "Single particle x-ray diffractive imaging," Nano Lett. **8**(1), 310–316 (2008).

Bogan, M. J., Starodub, D., Hampton, C. Y., and Sierra, R. G., "Single-particle coherent diffractive imaging with a soft x-ray free electron laser: Towards soot aerosol morphology," J. Phys. B: At. Mol. Opt. Phys. **43**(19), 194013 (2010).

Chapman, H. N., Barty, A., Bogan, M. J., Boutet, S., Frank, M., Hau-Riege, S. P., Marchesini, S., Woods, B., Bajt, S., Benner, H., London, R. A., Plonjes, E., Kuhlmann, M., Treusch, R., Du üsterer, S., Tschentscher, T., Schneider, J. R., Spiller, E., Moller, T., Bostedt, C., Hoener, M., Shapiro, D. A., Hodgson, K. O., van der Spoel, D., Burmeister, F., Bergh, M., Caleman, C., Huldt, G., Seibert, M. M., Maia, F. R. N. C., Lee, R. W., Szoke, A., Timneanu, N., and Hajdu, J., "Femtosecond diffractive imaging with a soft-x-ray free-electron laser," Nat. Phys. **2**(12), 839–843 (2006).

Chang, B. Y., Hoetzlein, R. C., and Mueller, J. A., "Improved two-dimensional product imaging: The real-time ion-counting method," Rev. Sci. Instrum. **69**(8), 1665–1670 (1998).

DePonte, D. P., Weierstall, U., Schmidt, K., Warner, J., Starodub, D., Spence, J. C. H., and Doak, R. B., "Gas dynamic virtual nozzle for generation of microscopic droplet streams," J. Phys. D-Appl. Phys. **41**(19), 195505 (2008).

Di Fonzo, F., Gidwani, A., Fan, M. H., Neumann, D., Iordanoglou, D. I., Heberlein, J. V. R., McMurry, P. H., Girshick, S. L., Tymiak, N., Gerberich, W. W., and Rao, N. P., "Focused nanoparticle-beam deposition of patterned microstructures," Appl. Phys. Lett. **77**(6), 910 (2000).

Ekeberg, T., Svenda, M., Abergel, C., Maia, F. R. N. C., Seltzer, V., Claverie, J.-M., Hantke, M., Jönsson, O., Nettelblad, C., van der Schot, G., Liang, M., DePonte, D. P., Barty, A., Seibert, M. M., Iwan, B., Andersson, I., Loh, N. D., Martin, A. V., Chapman, H., Bostedt, C., Bozek, J. D., Ferguson, K. R., Krzywinski, J., Epp, S. W., Rolles, D., Rudenko, A., Hartmann, R., Kimmel, N., and Hajdu, J., "Three-dimensional reconstruction of the giant mimivirus particle with an x-ray free-electron laser," Phys. Rev. Lett. **114**(9), 098102 (2015).

Fernandez de la Mora, J. and Rosell-Llompart, J., "Aerodynamic focusing of heavy molecules in seeded supersonic jets," J. Chem. Phys. **91**(4), 2603 (1989).

Frank, J., *Three-Dimensional Electron Microscopy of Macromolecular Assemblies: Visualization of Biological Molecules in Their Native State* (Oxford University Press, 2006).

Fuerstenau, S., Gomez, A., and Fernandez de la Mora, J., "Visualization of aerodynamically focused subsonic aerosol jets," J. Aerosol Sci. **25**(1), 165–173 (1994).

Gallagher-Jones, M., Bessho, Y., Kim, S., Park, J., Kim, S., Nam, D., Kim, C., Kim, Y., Noh, D. Y., Miyashita, O., Tama, F., Joti, Y., Kameshima, T., Hatsui, T., Tono, K., Kohmura, Y., Yabashi, M., Hasnain, S. S., Ishikawa, T., and Song, C., "Macromolecular structures probed by combining single-shot free- electron laser diffraction with synchrotron coherent x-ray imaging," Nat. Commun. **5**, 1–9 (2014).

Ganan-Calvo, A., "Generation of steady liquid microthreads and micron-sized monodisperse sprays in gas streams," Phys. Rev. Lett. **80**(2), 285–288 (1998).

Gomez, L. F., Ferguson, K. R., Cryan, J. P., Bacellar, C., Tanyag, R. M. P., Jones, C., Schorb, S., Anielski, D., Belkacem, A., Bernando, C., Boll, R., Bozek, J., Carron, S., Chen, G., Delmas, T., Englert, L., Epp, S. W., Erk, B., Foucar, L., Hartmann, R., Hexemer, A., Huth, M., Kwok, J., Leone, S. R., Ma, J. H. S., Maia, F. R. N. C., Malmerberg, E., Marchesini, S., Neumark, D. M., Poon, B., Prell, J., Rolles, D., Rudek, B., Rudenko, A., Seifrid, M., Siefermann, K. R., Sturm, F. P., Swiggers, M., Ullrich, J., Weise, F., Zwart, P., Bostedt, C., Gessner, O., and Vilesov, A. F., "Shapes and vorticities of superfluid helium nanodroplets," Science **345**(6199), 906–909 (2014).

Hantke, M. F., Hasse, D., Maia, F. R. N. C., Ekeberg, T., John, K., Svenda, M. *et al.*, "High-throughput imaging of heterogeneous cell organelles with an x-ray laser," Nat. Photonics **8**(12), 943–949 (2014).

Hawkes, P. and Spence, J. C. H., Eds., *Science of Microscopy* (Springer, New York, 2005).

Hoey, J. M., Lutfurakhmanov, A., Schulz, D. L., and Akhatov, I. S., "A review on aerosol-based direct-write and its applications for microelectronics," J. Nanotechnol. **2012**(9), 1–22.

Howells, M. R., Beetz, T., Chapman, H. N., Cui, C., Holton, J. M., Jacobsen, C. J., Kirz, J., Lima, E., Marchesini, S., Miao, H., Sayre, D., Shapiro, D. A., Spence, J. C. H., and Starodub, D., "An assessment of the resolution limitation due to radiation-damage in x-ray diffraction microscopy," J. Electron Spectrosc. Relat. Phenom. **170**(1–3), 4–12 (2009).

Israel, G. W. and Friedlander, S. K., "High-speed beams of small particles," J. Colloid Interface Sci. **24**(3), 330–337 (1967).

Jehle, J. A., Lange, M., Wang, H., Hu, Z., Wang, Y., and Hauschild, R., "Molecular identification and phylogenetic analysis of baculoviruses from Lepidoptera," Virology **346**(1), 180–193 (2006).

Küpper, J., Stern, S., Holmegaard, L., Filsinger, F., Rouzée, A., Rudenko, A., Johnsson, P., Martin, A. V., Adolph, M., Aquila, A., Bajt, S., Barty, A., Bostedt, C., Bozek, J., Caleman, C., Coffee, R., Coppola, N., Delmas, T., Epp, S., Erk, B., Foucar, L., Gorkhover, T., Gumprecht, L., Hartmann, A., Hartmann, R., Hauser, G., Holl, P., Hömke, A., Kimmel, N., Krasniqi, F., Kühnel, K.-U., Maurer, J., Messerschmidt, M., Moshammer, R., Reich, C., Rudek, B., Santra, R., Schlichting, I., Schmidt, C., Schorb, S., Schulz, J., Soltau, H., Spence, J. C. H., Starodub, D., Struder, L., Thøgersen, J., Vrakking, M. J. J., Weidenspointner, G., White, T. A., Wunderer, C., Meijer, G., Ullrich, J., Stapelfeldt, H., Rolles, D., and Chapman, H. N., "X-ray diffraction from isolated and strongly aligned gas-phase molecules with a free-electron laser," Phys. Rev. Lett. **112**(8), 083002 (2014).

La Mora, D., Fernández, J., and Riesco-Chueca, P., "Aerodynamic focusing of particles in a carrier gas," J. Fluid Mech. **195**, 1–21 (1988).
Liu, P., Ziemann, P., Kittelson, D., and McMurry, P., "Generating particle beams of controlled dimensions and divergence. I. Theory of particle motion in aerodynamic lenses and nozzle expansions," Aerosol Sci. Technol. **22**(3), 293–313 (1995).
Loh, N. D., Hampton, C. Y., Martin, A. V., Starodub, D., Sierra, R. G., Barty, A., Aquila, A., Schulz, J., Lomb, L., Steinbrener, J., Shoeman, R. L., Kassemeyer, S., Bostedt, C., Bozek, J., Epp, S. W., Erk, B., Hartmann, R., Rolles, D., Rudenko, A., Rudek, B., Foucar, L., Kimmel, N., Weidenspointner, G., Hauser, G., Holl, P., Pedersoli, E., Liang, M., Hunter, M. M., Gumprecht, L., Coppola, N., Wunderer, C., Graafsma, H., Maia, F. R. N. C., Ekeberg, T., Hantke, M., Fleckenstein, H., Hirsemann, H., Nass, K., White, T. A., Tobias, H. J., Farquar, G. R., Benner, W. H., Hau-Riege, S. P., Reich, C., Hartmann, A., Soltau, H., Marchesini, S., Bajt, S., Barthelmess, M., Bucksbaum, P., Hodgson, K. O., Struder, L., Ullrich, J., Frank, M., Schlichting, I., Chapman, H. N., and Bogan, M. J., "Fractal morphology, imaging and mass spectrometry of single aerosol particles in flight," Nature **486**(7404), 513–517 (2012).
Mallina, R. V., Wexler, A. S., and Johnston, M. V., "High-speed particle beam generation: Simple focusing mechanisms," J. Aerosol Sci. **30**(6), 719–738 (1999).
McDermott, G., Le Gros, M. A., and Larabell, C. A., "Visualizing cell architecture and molecular location using soft x-ray tomography and correlated cryo-light microscopy," Annu. Rev. Phys. Chem. **63**(1), 225–239 (2012).
Murphy, W. K. and Sears, G. W., "Production of particulate beams," J. Appl. Phys. **35**(6), 1986–1987 (1964).
Nelson, A. J., Toleikis, S., Chapman, H., Bajt, S., Krzywinski, J., Chalupský, J., Juha, L., Cihelka, J., Hájková, V., Vysin, L., Burian, T., Kozlova, M., Fäustlin, R. R., Nagler, B., Vinko, S. M., Whitcher, T., Dzelzainis, T., Renner, O., Saksl, K., Khorsand, A. R., Heimann, P. A., Sobierajski, R., Klinger, D., Jurek, M., Pelka, J., Iwan, B., Andreasson, J., Timneanu, N., Fajardo, M., Wark, J. S., Riley, D., Tschentscher, T., Hajdu, J., and Lee, R. W., "Soft x-ray free electron laser microfocus for exploring matter under extreme conditions," Opt. Express **17**(20), 18271–18278 (2009).
Neutze, R., Wouts, R., van der Spoel, D., Weckert, E., and Hajdu, J., "Potential for biomolecular imaging with femtosecond x-ray pulses," Nature **406**(6797), 752–757 (2000).
Nugent, K. A., "Coherent methods in the x-ray sciences," Adv. Phys. **59**(1), 1–99 (2010).
Qi, L., McMurry, P. H., Norris, D. J., and Girshick, S. L., "Micropattern deposition of colloidal semiconductor nanocrystals by aerodynamic focusing," Aerosol Sci. Technol. **44**(1), 55–60 (2010).
Rao, N. P., Navascues, J., and Fernandez de la Mora, J., "Aerodynamic focusing of particles in viscous jets," J. Aerosol Sci. **24**(7), 879–892 (1993).
Robinson, A., "On the motion of small particles in a potential field of flow," Commun. Pure Appl. Math. **9**(1), 69–84 (1956).
Rupp, D., Adolph, M., Flückiger, L., Gorkhover, T., Müller, J. P., Müller, M., Sauppe, M., Wolter, D., Schorb, S., Treusch, R., Bostedt, C., and T. Möller, "Generation and structure of extremely large clusters in pulsed jets," J. Chem. Phys. **141**(4), 044306 (2014).
Seibert, M. M., Ekeberg, T., Maia, F. R. N. C., Svenda, M., Andreasson, J., Jonsson, O., Odic, D., Iwan, B., Rocker, A., Westphal, D., Hantke, M., Deponte, D. P., Barty, A., Schulz, J., Gumprecht, L., Coppola, N., Aquila, A., Liang, N. M., White, T. A., Martin, A., Caleman, C., Stern, S., Abergel, C., Seltzer, V., Claverie, J. M., Bostedt, C., Bozek, J. D., Boutet, S., Miahnahri, A. A., Messerschmidt, M., Krzywinski, J., Williams, G., Hodgson, K. O., Bogan, M. J., Hampton, C. Y., Sierra, R. G., Starodub, D., Andersson, I., Bajt, S., Barthelmess, M., Spence, J. C. H., Fromme, P., Weierstall, U., Kirian, R., Hunter, M., Doak, R. B., Marchesini, S., Hau-Riege, S. P., Frank, M., Shoeman, R. L., Lomb, L., Epp, S. W., Hartmann, R., Rolles, D., Rudenko, A., Schmidt, C., Foucar, L., Kimmel, N., Holl, P., Rudek, B., Erk, B., Homke, A., Reich, C., Pietschner, D., Weidenspointner, G., Struder, L., Hauser, G., Gorke, H., Ullrich, J., Schlichting, I., Herrmann, S., Schaller, G., Schopper, F., Soltau, H., Kuhnel, K. U., Andritschke, R., Schroter, C. D., Krasniqi, F., Bott, M., Schorb, S., Rupp, D., Adolph, M., Gorkhover, T., Hirsemann, H., Potdevin, G., Graafsma, H., Nilsson, B., Chapman, H. N., and Hajdu, J., "Single mimivirus particles intercepted and imaged with an x-ray laser," Nature **470**(7332), 78–82 (2011).
Suga, M., Akita, F., Hirata, K., Ueno, G., Murakami, H., Nakajima, Y., Shimizu, T., Yamashita, K., Yamamoto, M., Ago, H., and Shen, J.-R., "Native structure of photosystem II at 1.95 A resolution viewed by femtosecond x-ray pulses," Nature **517**(7532), 99–103 (2015).
Tenboer, J., Basu, S., Zatsepin, N., Pande, K., Milathianaki, D., Frank, M., Hunter, M., Boutet, S., Williams, G. J., Koglin, J. E., Oberthuer, D., Heymann, M., Kupitz, C., Conrad, C., Coe, J., Roy-Chowdhury, S., Weierstall, U., James, D., Wang, D., Grant, T., Barty, A., Yefanov, O., Scales, J., Gati, C., Seuring, C., Srajer, V., Henning, R., Schwander, P., Fromme, R., Ourmazd, A., Moffat, K., Van Thor, J. J., Spence, J. C. H., Fromme, P., Chapman, H. N., and Schmidt, M., "Time-resolved serial crystallography captures high-resolution intermediates of photoactive yellow protein," Science **346**(6214), 1242–1246 (2014).
van der Schot, G., Svenda, M., Maia, F. R. N. C., Hantke, M., DePonte, D. P., Seibert, M. M., Aquila, A., Schulz, J., Kirian, R., Liang, M., Stellato, F., Iwan, B., Andreasson, J., Timneanu, N., Westphal, D., Almeida, F. N., Odic, D., Hasse, D., Carlsson, G. H., Larsson, D. S. D., Barty, A., Martin, A. V., Schorb, S., Bostedt, C., Bozek, J. D., Rolles, D., Rudenko, A., Epp, S., Foucar, L., Rudek, B., Hartmann, R., Kimmel, N., Holl, P., Englert, L., Loh, N.-T. D., Duane Loh, N.-T., Chapman, H. N., Andersson, I., Hajdu, J., and Ekeberg, T., "Imaging single cells in a beam of live cyanobacteria with an x-ray laser," Nat. Commun. **6**, 5704–5709 (2015).
Vidal-de-Miguel, G. and de la Mora, J. F., "Continuously converging multistage focusing lenses to concentrate aerosols at high Reynolds numbers," Aerosol Sci. Technol. **46**(3), 287–296 (2012).
Wang, X. and McMurry, P. H., "A design tool for aerodynamic lens systems," Aerosol Sci. Technol. **40**(5), 320–334 (2006a).
Wang, X. and McMurry, P. H., "An experimental study of nanoparticle focusing with aerodynamic lenses," Int. J. Mass Spectrom. **258**(1–3), 30–36 (2006b).
Xu, R., Jiang, H., Song, C., Rodriguez, J. A., Huang, Z., Chen, C.-C., Nam, D., Park, J., Gallagher-Jones, M., Kim, S., Kim, S., Suzuki, A., Takayama, Y., Oroguchi, T., Takahashi, Y., Fan, J., Zou, Y., Hatsui, T., Inubushi, Y., Kameshima, T., Yonekura, K., Tono, K., Togashi, T., Sato, T., Yamamoto, M., Nakasako, M., Yabashi, M., Ishikawa, T., and Miao, J., "Single-shot three-dimensional structure determination of nanocrystals with femtosecond x-ray free-electron laser pulses," Nat. Commun. **5**, 4061 (2014).